GEOPHYSICAL RESEARCH LETTERS, VOL. 22, NO. 16, PAGES 2253-2256, AUGUST 15, 1995

Source time function of the great 1994 Bolivia deep earthquake by waveform and spectral inversions

Pierre F. Ihmlé
Département de Sismologie, Institut de Physique du Globe, Paris

Thomas H. Jordan
Department of Earth, Atmospheric and Planetary Sciences, MIT, Cambridge

Abstract. The source time function of the great 1994 Bolivia deep earthquake is estimated from far-field seismograms by two techniques: time-domain inversion of direct *P* and *S* waveforms, and spectral-domain inversion of a combination of body waves, first-orbit traveling modes, and free oscillations. Both methods give consistent estimates, but the latter provides more bandwidth (1-300 mHz) and is more robust with respect to source-directivity effects and wave scattering. The earthquake released a total moment of 2.7 ($\pm$ 0.1) $\times$ 10^{21} Nm over an interval of about 50 s. Its history is highly episodic and can be divided into three stages: an initial sequence ($0 \lesssim t \lesssim 13$ s; 2×10^{20} Nm), a main-event sequence ($13 \lesssim t \lesssim 38$ s; 2.2×10^{21} Nm), and a terminal sequence ($38 \lesssim t \lesssim 50$ s; 3×10^{20} Nm). The main event is resolved into five subevents with peaks at ~ 16, 20, 26, 29, and 36 s. The spatial pattern of moment release suggests that the main event was confined to the cold slab core, while the initial and terminal stages were part of a distinct westward-propagating rupture in the lower reaches of the former oceanic plate.

Introduction

The Bolivia earthquake of 9 Jun 94 was a very large, deep event (M_W = 8.3, h = 657 km), well recorded by high-performance seismic stations (Kikuchi and Kanamori, 1994), including close-in temporary arrays (Silver et al., 1995). It therefore makes a good test case for methods of estimating source parameters from far-field data. Here we focus on the recovery of its source time function $f(t)$. For an arbitrary event with a Backus stress-glut-rate tensor $\dot{\Gamma}(\mathbf{r},t)$ extended over a volume V and interval $[t_0,t_\infty]$, this scalar function is defined by

$$f(t) = \frac{1}{\sqrt{2}} \int_V \hat{\mathbf{M}} : \dot{\Gamma}(\mathbf{r},t)\, d\mathbf{r}, \quad t \in [t_0,t_\infty], \tag{1}$$

where $\hat{\mathbf{M}} = (\sqrt{2}\, M_T^0)^{-1} \int_V \Gamma(\mathbf{r},t_\infty)\, d\mathbf{r}$ is the normalized source mechanism tensor. We have applied two procedures to seismograms recorded at the stations shown in Figure 1: *waveform inversion*, which estimates $f(t)$ directly from broadband recordings of direct *P* and *S* waves, and *spectral synthesis and inversion*, which first combines separate analyses of body phases, traveling modes, and free oscillations to estimate the source spectrum $f(\omega)$ and then inverts this spectrum for $f(t)$. In both cases, we assumed that the source time function was non-negative and that $\hat{\mathbf{M}}$ was well approximated by the Harvard CMT mechanism (which agreed with our own moment-tensor solution).

Paper number 95GL01437
0094-8534/95/95GL-01437$03.00

Waveform Inversion

Many waveform-inversion methods have been published, some relying on the generalized deconvolution of *P* waves for $f(t)$ (e.g., Hartzell and Heaton, 1985; Ruff, 1989) and others involving more complex optimization schemes to constrain spatial as well as temporal variability (e.g., Ekström, 1989; Kikuchi and Kanamori, 1991). Our procedure, which is of the former type, is illustrated in Figure 2. For each broadband *P* or *S* waveform $u_n(t)$ observed at the nth station, a synthetic waveform $\tilde{u}_n(t)$ was calculated assuming a unit step at the source centroid $\mathbf{r}_0$. An estimate of the source time function was found by minimizing the quadratic form

$$\varepsilon^2(f) = \cos\theta \int_{t_0}^{t_\infty} [u_n(t) - \tilde{u}_n(t) * f(t)]^2\, dt + \sin\theta \int_{t_0}^{t_\infty} [\dot{f}(t)]^2\, dt, \tag{2}$$

subject to two constraints: the one-sided condition, $f(t) \geq 0$, and a total-moment normalization, $\int_{t_0}^{t_\infty} f(t)\, dt = M_T^0$. The two terms in (2) measured the waveform misfit and the smoothness of $f(t)$, respectively, and the adjustable tradeoff parameter $\theta \in (0,\pi/2)$ governed their relative weight. The side conditions stabilized the inversion (Hartzell and Heaton, 1985; Ekström, 1989); the first is a physical constraint (no net backslip), whereas the second requires additional information. We assumed a total moment of $M_T^0 = 2.7 \times 10^{21}$ Nm, derived from the low-frequency spectra presented below, and performed the inversions using a quadratic-programming algorithm of Lawson and Hanson (1974; coded by R. L. Parker and P. Stark). The samples obtained by this minimization, $\{\tilde{f}_n(t) : n = 1,...,N\}$, were cross-correlated and time-shifted to optimize their mutual alignment, and their median value was computed at each time point (median-stacked) to yield a network estimate $\tilde{f}(t)$ (Figure 3).

Good quality *P* waveforms on vertical (Z) components and *S* waveforms on transverse (T) components were selected from

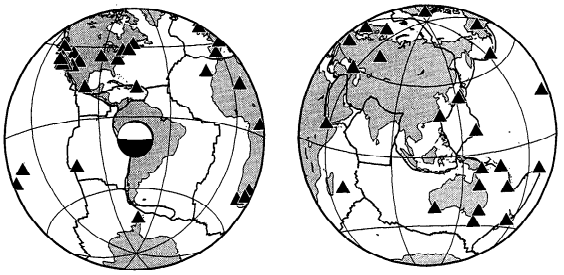

Figure 1. Lambert projections centered on the epicenter showing the Harvard CMT focal mechanism and the 50 seismic stations (triangles) used in this study.

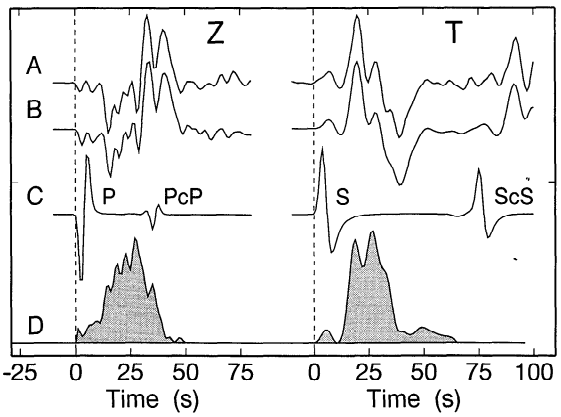

Figure 2. Examples of waveform inversions of broadband seismograms recorded at station TUC (Δ = 62°, ϕ = 319°). Line A shows the observed *P* wave on the vertical component (Z) and *S* wave on the transverse component (T); line B shows synthetic seismograms produced by convolving WKBJ responses for a point source (line C) with the source time functions obtained by minimization of equation (2) (line D). A sinc^4 filter with first node at 500 mHz was applied to both data and transfer functions prior to inversion. Zero time is the *P*-wave origin time (UT 94:06:09:00:33:19.1).

stations at epicentral distances of 30-90°, and synthetics were computed from the *iasp91* velocity model and PREM attenuation model by Chapman's WKBJ method. Although the *P*-wave and *S*-wave solutions display considerable variability, caused primarily by the spatial complexity of the moment release, the resulting Z and T median stacks are similar (Figure 3). They both show an initiation of moment release near the high-frequency origin time (t = 0), which accelerates at ~13 s into a main episode that is characterized by primary peaks near 20 s and 29 s. The Z stack is somewhat rougher, with additional peaks at 26 s and 36 s and a shoulder at 16 s; it decays to zero at about 50 s, while the T stack has a tail extending to 60 s. The latter feature is needed to match the second swing of the *S*-wave, as illustrated in Figure 2.

Spectral Synthesis and Inversion

We employ the procedure of Ihmlé et al. (1993), which is based on the Fourier relationship $f(\omega) = A(\omega)e^{i\omega\Delta t(\omega)} = \int_{-\infty}^{+\infty} f(t)e^{i\omega(t-t_0)}\,dt$. The polar form of $f(\omega)$ defines two real-valued, even functions of frequency: an amplitude spectrum $A(\omega)$, which is non-negative, and a phase-delay spectrum $\Delta t(\omega)$, which is referenced to the high-frequency origin time t_0. Estimates A_{nj} and Δt_{nj} for the nth station were extracted at a set of discrete frequencies $\{\omega_j : j=1,\ldots,J\}$ in a series of overlapping bands from four data types: (1) free oscillations [6-hr records; 1-10 mHz], (2) first-orbit fundamental- and higher-mode surface waves [1-hr records; 2-20 mHz], (3) long-period body wavetrains [5-min records; 10-50 mHz], (4) broadband *P* and *S* phases [3–4-min records; 15-300 mHz]. The differential amplitudes and phase delays of these data were measured relative to synthetic waveforms by the techniques described by Jordan (1991) and Ihmlé et al. (1993). For data sets (1)-(3), the synthetics were computed by complete mode summation from the anisotropic version of PREM and corrected by an asymptotic theory for aspherical structure up to spherical harmonic degree 12 using model SH12/WM13 of Su et al. (1994); for fundamental modes above 7 mHz, these corrections were extended to higher-order heterogeneity using the degree-36 phase-velocity maps of Ekström et al. (1993). Data set (4) was derived using WKBJ synthetics computed from the *iasp91* model. The PREM attenuation model was used in all cases. The spectral data from individual records were median-stacked over all N stations to obtain the network estimates A_j and Δt_j, which were then combined to form the complex number $f_j = A_j e^{i\omega_j \Delta t_j}$. The network estimate of the source time function was found by minimizing the quadratic form

$$\varepsilon^2(f) = \cos\theta \sum_{j=1}^{J} \sigma_j^{-2} \left| f_j - \int_{t_0}^{t_-} f(t) e^{i\omega_j (t-t_0)}\,dt \right|^2 + \sin\theta \int_{t_0}^{t_-} [\dot{f}(t)]^2\,dt, \qquad (3)$$

subject to the one-sided condition, $f(t) \geq 0$.

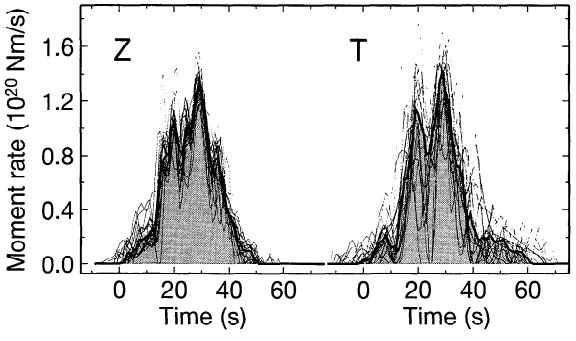

Figure 3. Source time functions obtained by waveform inversion of broadband seismograms. Thin lines show results for 22 vertical-component *P* waves (Z) and 21 transverse-component *S* waves (T) recorded at epicentral distances from 30° to 95°, after alignement by cross-correlation. Thick lines are the median values at each time point (median stacks).

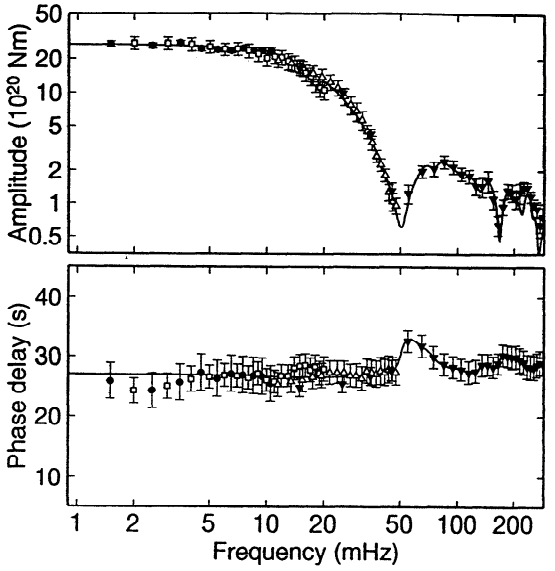

Figure 4. Amplitude (top panel) and phase-delay (bottom panel) spectra of the source time function. Points with 1-σ error bars are network averages for four data types: free oscillations (solid circles), first-orbit traveling modes (open squares), long-period body wavetrains (open triangles), and broad-band *P* and *S* phases (solid triangles). Solid line is calculated from the Z+T source time function of Figure 5. Amplitude and frequency scales are logarithmic. Zero phase delay time corresponds to the *P*-wave origin time.

Spectra were derived separately for the Z and T seismograms over a bandwidth spanning two and a half orders of magnitude (1-300 mHz). A simple average of these two independent estimates yielded the data plotted in Figure 4, which were inverted to obtain the Z+T solution in Figure 5. The observed amplitude spectrum is flat from 1 to 10 mHz, where it begins to roll off smoothly into a well-defined spectral hole at about 50 mHz; this hole corresponds to a 5-s step in the phase-delay spectrum, which is very flat below 50 mHz. The amplitude has a second hole at about 170 mHz, corresponding to another, smaller jump in phase delay, and there is an indication of a third hole near the upper end of the frequency band. The Z+T solution fits the data quite well except at frequencies greater than 200 mHz, where it slightly underpredicts the amplitudes, and less than 5 mHz, where it slightly overpredicts the phase delays. The spectral intercepts and curvatures at zero frequency correspond to integral properties of the source time function (Jordan, 1991); the Z+T solution has a total moment of M_T^0 = 2.68 (± 0.10) × 10^{21} Nm, a centroid time shift of Δt_1 = 24.2 ± 1.0 s, a characteristic duration of τ_c = 21.2 ± 0.7 s, and a time-function skewness parameter of α = 0.0 ± 0.1.

The residuals of the individual Z and T data sets with respect to the Z+T solution (Figure 6) can be represented as the real and imaginary parts of the complex number

$$\frac{1}{\omega_j}\ln[f_j / \tilde{f}(\omega_j)] \equiv \delta\tau_p(\omega_j) + i\,\delta\tau_q(\omega_j), \qquad (4)$$

Here we have followed the notation and conventions in Gee and Jordan's (1992) treatment of generalized data functionals: the real part is just the difference between the observed and computed phase delays, $\delta\tau_p(\omega_j) = \Delta t_j - \Delta\tilde{t}(\omega_j)$, whereas the imaginary part is proportional to the difference in the logarithmic amplitudes, $\delta\tau_q(\omega_j) = -\omega_j^{-1}[\ln A_j - \ln\tilde{A}(\omega_j)]$. The latter is an appropriate measure of misfit for seismic amplitudes, whose statistical variations are known to be approximated by a log-normal distribution (e.g., Ruff, 1989). The residuals show some significant and potentially interesting differences between the Z and T components; for example, at frequencies less than about 8 mHz, $\delta\tau_p$ is systematically less for Z than T by a few seconds, which may be a bias related to velocity structure, and, in the band from 25 to 170 mHz, $\delta\tau_q$ is systematically greater for Z by about a second, which may be a bias related to attenuation structure. However, the scatter in $\delta\tau_q$ at a fixed frequency has approximately the same absolute amplitude as the scatter in $\delta\tau_p$. This rough equality,

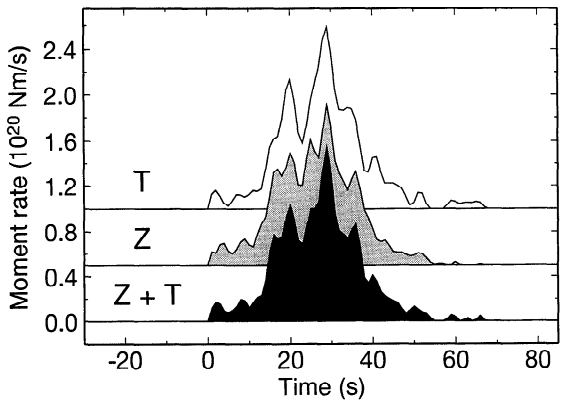

Figure 5. Source time functions obtained by the inversion of network-averaged spectra from transverse (T), vertical (Z), and both (Z+T) components. The first two are vertically shifted for clarity. Zero time is the *P*-wave origin time.

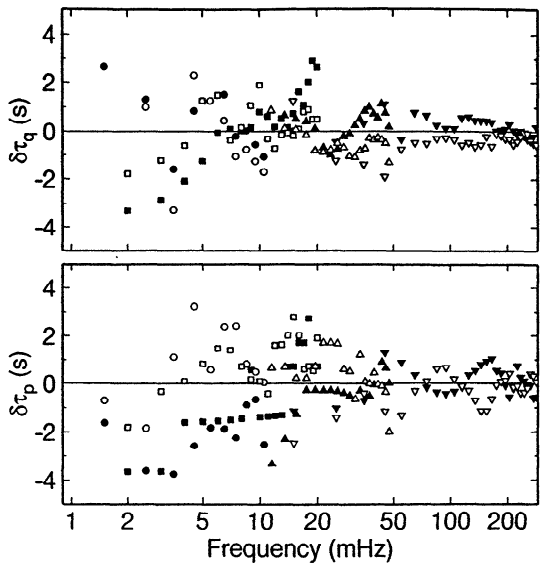

Figure 6. Spectral residuals of the network-averaged Z (solid symbols) and T (open symbols) data with respect to the Z+T solution of Figure 5, plotted as $\delta\tau_q$ (top panel) and $\delta\tau_p$ (bottom panel) for free oscillations (circles), first-orbit traveling modes (squares), long-period body wavetrains (triangles), and broad-band *P* and *S* phases (inverted triangles). Frequency scale is logarithmic.

which is maintained across the entire frequency band, may reflect the statistics of scattering by small-scale heterogeneities. For example, Rytov theory predicts equality in the Fraunhofer limit where the scatterer size is much smaller than the geometric mean of the wavelength and path length (Chernov, 1960). This scaling supports the use of $\delta\tau_p$ and $\delta\tau_q$ as data functionals in spectral synthesis and inversion.

Source time functions resulting from the inversion of the Z, T, and Z+T spectral estimates are compared in Figure 5. Given the differences in the data sets, the Z and T solutions are very consistent, not only in terms of their integral parameters (M_T^0 = 2.65 vs. 2.70 × 10^{21} Nm; Δt_1 = 23.4 vs. 25.4 s; τ_c = 20.7 vs. 20.9 s; α = 0.0 vs. 0.0), but also in the details of the episodicity revealed by the amplitude and timing of the moment-release peaks. In the main-rupture sequence extending from about 13 to 38 s, the Z solution has five such peaks, each corresponding to a similar feature in the Z solution of Figure 3. As in the case of the time-domain analysis, the T solution is somewhat smoother; e.g., the peaks in Z at 16 and 26 s are evident only as shoulders on the larger peaks at 20 and 29 s. But the differences are minor, and the agreement is better than in Figure 3, especially during the terminal stage of the moment release after 38 s.

Discussion

The Bolivia earthquake proceeded in three stages: (I) an initial sequence ($0 \lesssim t \lesssim 13$ s; 2×10^{20} Nm), (II) a main-event sequence ($13 \lesssim t \lesssim 38$ s; 2.2×10^{21} Nm), and (III) a terminal sequence ($38 \lesssim t \lesssim 50$ s; 3×10^{20} Nm). Our analysis resolves the main rupture into five subevents with moment-rate peaks at approximately 16, 20, 26, 29, and 36 s, which is roughly consistent with the event structure observed at close-in stations (Silver et al., 1995). We picked the subevent peak times on the source time functions recovered by waveform inversion of individual *P*-wave seismograms, and we were able

to deduce from their relative locations that the Stage-II sequence propagated along the nearly horizontal nodal plane in an eastward and northward direction from the Stage-I hypocenter over an area with a linear dimension of about 50 km, in agreement with previous authors (Kikuchi and Kanamori, 1994; Silver et al., 1995). The implications of this rupture pattern for the mechanics of deep-focus earthquakes have been explored by Silver et al. (1995), who point out the inconsistency of the geometry with transformational-faulting theories (Green et al., 1990) that confine deep ruptures to a thin wedge of metastable olivine at the cold core of the descending slab. They speculate that the earthquake initiated in the lower (now southern) part of the subducted plate and propagated along an old zone of weakness.

We also used the waveform-inversion results in a time-domain analysis of the Stage-III rupture, and we found that its cutoff was located about 40 km *west* of the Stage-I hypocenter. Stations at easterly azimuths, for example, have source time functions with total durations that are approximately 4 s greater than stations to the west. This geometry, combined with the observation that the moment-release rates for Stages I and III are roughly equal, suggests that these two stages may mark the beginning and the end, respectively, of a continuous, westward-propagating rupture that was distinct from the main event. Building on Silver et al.'s (1995) hypothesis, we can speculate that the main event, which involved a high rate of moment release that may have been confined to the cold slab core, was initiated by a smaller, more temporally extended rupture in the lower reaches of the former oceanic plate.

Both of the methodologies employed here give consistent estimates of the Bolivia source time function, but spectral synthesis and inversion has two distinct advantages over time-domain waveform inversion. First, the spectral method incorporates normal-mode and surface-wave information at frequencies less than 10 mHz, well below the range achievable from the individual body phases employed in waveform inversions (Ekström, 1989). The low-frequency information is especially important for fixing the integral properties of $f(t)$, such as total moment, centroid time, and characteristic duration, which are crucial for understanding large earthquakes of long duration (Ihmlé and Jordan, 1994). Second, network stacking of the differential parameters $\delta\tau_p$ and $\delta\tau_q$ yields robust spectral estimates. In particular, this type of averaging appears to be very effective in reducing the signal-generated noise associated with source directivity and small-scale heterogeneities without introducing significant bias. Its efficacy in this regard is attested to by the consistency of all four data sets—free oscillations, surface waves, body wavetrains, direct phases—for both Z and T components (see Figures 4 and 6). Network stacking in the time domain is not so straightforward; realignments are needed to account for travel-time variations, and source directivity effects can lead to incoherencies that cause distortions in the recovered source time functions. The latter is relatively small for the Bolivia deep earthquake, as indicated by the good agreement between the time-domain and spectral-domain results obtained here, but the same cannot be said for many large, shallow-focus events.

Acknowledgments. We thank G. Ekström, J. Tromp, and E. Larson for use of their unpublished phase-velocity maps and R. Cicerone for assistance. This research was sponsored by the National Science Foundation under grant EAR-9305081.

References

Chernov, L. A., *Wave Propagation in Random Media*, Dover, New York, 168 pp., 1960.

Ekström, G., A very broad band inversion method for the recovery of earthquake source parameters, *Tectonophysics*, **166**, 73-100, 1989.

Ekström, G., J. Tromp, and E. Larson, Measurements and models of global surface wave propagation (abstract), *Eos*, **74**, 438, 1993.

Gee, L., and T. H. Jordan, Generalized seismological data functionals, *Geophys. J. Int.*, **111**, 363-390, 1992.

Green, H. W., and P. C. Burnley, A new self-organizing mechanism for deep-focus earthquakes, *Nature*, **341**, 733-737, 1989.

Ihmlé, P. F., P. Harabaglia, and T. H. Jordan, Teleseismic detection of a slow precursor to the great 1989 Macquarie Ridge earthquake, *Science*, **261**, 177-183, 1993.

Ihmlé, P. F., and T. H. Jordan, Teleseismic search for slow precursors to large earthquakes, *Science*, **266**, 1547-1551, 1994.

Jordan, T. H., Far-field detection of slow precursors to fast seismic ruptures, *Geophys. Res. Lett.*, **18**, 2019-2022, 1991.

Kikuchi, M., and H. Kanamori, Inversion of complex body waves – III, *Bull. Sesim. Soc. Am.*, **81**, 2335-2350, 1991.

Kikuchi, M., and H. Kanamori, The mechanism of the deep Bolivia earthquake of June 9, 1994, *Geophys. Res. Lett.*, **21**, 2341-2344, 1994.

Lawson, C. L., and R. J. Hanson, *Solving Least Squares Problems*, Prentice-Hall, Englewood Cliffs, NJ, pp. 160-165, 1974.

Ruff, L. J., Multi-trace deconvolution with unknown trace scale factors: omnilinear inversion of *P* and *S* waves for source time functions, *Geophys. Res. Lett.*, **16**, 1043-1046, 1989.

Silver, P. G., S. L. Beck, T. C. Wallace, C. Meade, S. C. Meyers, D. E. James, and R. Kuehnel, Rupture characteristics of the deep Bolivian earthquake of 9 June 1994 and the mechanism of deep-focus earthquakes, *Science*, **268**, 69-73, 1995.

Su, W.-J., R. L. Woodward, and A. M. Dziewonski, Degree 12 model of shear velocity heterogeneity in the mantle, *J. Geophys. Res.*, **99**, 6945-6980, 1994.

P. F. Ihmlé, Département de Sismologie, Institut de Physique du Globe, 4 Place Jussieu, 75252 Paris Cedex 05, France.

T. H. Jordan, Department of Earth, Atmospheric and Planetary Sciences, 54-918, MIT, Cambridge, MA 02139, U.S.A..

(Received January 20, 1995; accepted March 30, 1995.)